Water-assisted formation of amine-bridged carbon nitride: A structural insight into the photocatalytic performance for H₂ evolution under visible light

Dawoon Jang [a], Seungjoo Choi [a], Nam Hee Kwon [b], Kyung Yeon Jang [c], Suyeon Lee [a], Tae-Woo Lee [c,d], Seong-Ju Hwang [b], Hyungjun Kim [e], Jeongho Kim [a,*], Sungjin Park [a,*]

[a] Department of Chemistry and Chemical Engineering, Inha University, 100 Inha-ro, Michuhol-gu, Inheon 22212, Republic of Korea
[b] Department of Materials Science and Engineering, College of Engineering, Yonsei University, 50 Yonsei-ro, Seodaemun-gu, Seoul 03722, Republic of Korea
[c] Department of Materials Science and Engineering, Seoul National University, 1 Gwanak-ro, Gwanak-gu, Seoul 08826, Republic of Korea
[d] School of Chemical and Biological Engineering, Institute of Engineering Research, Research Institute of Advanced Materials, Soft Foundry, Seoul National University, 1 Gwanak-ro, Gwanak-gu, Seoul 08826, Republic of Korea
[e] Department of Chemistry and Research Institute of Basic Sciences, Incheon National University, 119 Academy-ro, Yeonsu-gu, Incheon 22012, Republic of Korea

ARTICLE INFO

ABSTRACT

Carbon nitride (C₃N₄) exhibits significant potential as a metal-free photocatalyst for H₂ production using visible light. While the C₃N₄ network consists of tri-*s*-triazine building units linked by H bonds, it is still controversial how the H bonds affect the photocatalytic performance. In this study, we present a water-assisted method for production of polymeric carbon nitride to control intraplanar structures associated with H bonds and amine bridges. The C₃N₄ samples produced with a thermal treatment using water and humidified air gas (CN-H) exhibit excellent photocatalytic activities for the hydrogen evolution reaction. From structural and photophysical characterizations, it is found that CN-H samples contain fewer H bonds and more amine bridging groups as well as possess larger domains than C₃N₄ samples produced without using water (CN-A). These structural changes induced by the water treatment lead to efficient intraplanar migration of photoexcited charge carriers and thus are responsible for the enhanced photocatalytic performances.

1. Introduction

Carbon nitrides (C₃N₄s) refer to various chemical derivatives comprising C and N atoms. Polymeric C₃N₄ (p-C₃N₄), also known as graphitic carbon nitride (g-C₃N₄), is the most stable carbon nitride structure [1–5]. C₃N₄-based materials exhibit excellent chemical and optical properties, such as dispersibility in a two-dimensional (2D) form, bandgap at visible wavelengths, high-yield fluorescence, biocompatibility, and low cost [6–8]. Given these properties, C₃N₄s have attracted considerable interest as materials suitable for various applications, such as in photocatalysts [9–11], light-emitting diodes [12,13], bioimaging probes [14], photosensors [15], gas adsorbents [16,17], and supports for photo (electro)catalysts [18,19]. In particular, C₃N₄s exhibit great potential as efficient, metal-free, and eco-friendly photocatalysts for hydrogen evolution reactions (HERs) by water splitting and are potentially compatible with conventional metal-containing semiconductors

used for photocatalytic HER [20–22].

C₃N₄ materials are commonly produced by the solid-state thermal polycondensation of C, N-containing organic precursors. Although the porosity and crystallinity of the synthesized C₃N₄s vary depending on the type of organic precursor, the C, N alternating tri-*s*-triazine ring is a basic intralayer building unit of the C₃N₄ network [23–25]. As-prepared C₃N₄s typically have a three-dimensional (3D) structure with 2D layers stacked by interlayer interactions such as van der Waals forces and π-π interactions. When polymerization is completed, the tri-*s*-triazine rings are linked through amine bridges formed with the loss of ammonia [26].

However, polycondensation is often incomplete, leading to the formation of a partially condensed C₃N₄ network with heterogeneity and low crystallinity [27]. Such limitations have prevented a complete understanding of the precise chemical structures. Experimental characterizations using solid-state nuclear magnetic resonance (SSNMR) spectroscopy, electron diffraction measurements, and theoretical

calculations revealed that the partially condensed oligomeric melon strands are linked through hydrogen bonds between H atoms in the terminal amine groups and N atoms in the tri-*s*-triazine rings, forming 2D structures with long-range order. Although the H bonds play a critical role in bridging the intralayer building units forming the 2D structure [28,29], they may obstruct the intralayer migration of the photogenerated charge carriers through the entire 2D network and, consequently, accelerate the recombination of localized charge carriers within each strand, thus eventually reducing the photocatalytic activity of the materials [30,31]. Therefore, the relevant modification of the structures associated with H bonds is crucial for controlling their photophysical and photocatalytic properties.

Although recent studies have investigated the role of H bonds interconnecting the C_3N_4 network, it is still controversial how H bonds affects the chemical structure, photophysical properties, and photocatalytic performance of C_3N_4s. For example, Wu et al. prepared C_3N_4 materials at various temperatures between 550 and 650 °C and revealed that C_3N_4s produced at 650 °C contained fewer H bonds [32]. In particular, C_3N_4s with fewer H bonds exhibited enhanced photocatalytic properties for the degradation of organic pollutants. However, in the C_3N_4s prepared at 650 °C, the amount of H bonds was reduced, but more amine bridging groups were produced between the tri-*s*-triazine rings, according to structural characterization via ^{13}C SSNMR spectroscopy. Zhang et al. reported that a two-step heat treatment can reduce the amount of H bonds [33]. Intralayer H bonds were generated between the tri-*s*-triazine rings during the first heat treatment at 520 °C. The second heat treatment at 620 °C broke the H bonds, leading to the formation of more amine bridges. This two-step heat treatment resulted in the formation of a longer conjugated network with better crystallinity and higher long-range order, leading to improved photocatalytic activity for the HER. Another study using a two-step heating process showed that efficient HER photocatalysts were produced through the breakage of H bonds [30]. However, the proposed structural mechanism of C_3N_4 formation differs from that suggested in the above-mentioned works. Based on this previous report, the intralayer long-range order was broken by the partial loss of the N atoms during the second heating process, resulting in the introduction of mid-gap states and a red shift in light absorption, ultimately leading to improved photocatalytic activities.

Herein, we developed a novel and facile H_2O-assisted method to control the structure of the C_3N_4 networks associated with the H bonds and produce efficient photocatalysts for HER under visible light irradiation. In particular, the heat treatment of water-treated melamine under humidified air gas produced p-C_3N_4 materials with fewer H bonds and more amine bridging groups, leading to improved performance for photocatalytic HER. In addition, we revealed the relationships between the chemical structures, photophysical properties, and photocatalytic activities of the resulting p-C_3N_4 with various chemical and photophysical characteristics, including SSNMR, 2D excitation-emission map (2D EEM), and time-resolved photoluminescence (TR-PL) spectroscopy. The overall photocatalytic performance associated with the H bonds and amine bridges was comprehensively investigated by considering various factors such as crystallinity, thermal stability, surface area, porosity, bandgap, visible light absorption ability, lifetimes of photoexcited charge carriers, charge transfer resistances at the interfaces, and uniform formation of co-catalysts at the surface of the p-C_3N_4 network.

2. Experimental section

2.1. Preparation of water-treated p-C_3N_4

Melamine powder (5 g, Aldrich, 99%) was loaded into a quartz crucible filled with deionized (DI) water (3 mL). The crucible was placed at the center of a tube furnace and heated to one of the specified temperatures (550, 600, and 650 °C) at a heating rate of 5 °C/min. During the heating process, a mixture gas of H_2O and air was continuously flowed through the tube by bubbling the air through the DI water (130

mL) using an air pump. The flow rate of the humidified air was 221 L/min, and the humidity in the furnace at room temperature was 93% on average. The humidity at the elevated temperatures (550, 600, and 650 °C) could not be measured because the commercial hygrometer (Thermo-Hygrometer, SK-110TRHII, Type 1, SATO, Tokyo, Japan) can be broken at such high temperatures. After the crucible was retained in the furnace at an elevated temperature for 4 h, the tube was cooled to 25 °C. The resultant materials in the crucible were ground using a mortar and pestle, yielding powdered products (denoted as CN550-H, CN600-H, and CN650-H, depending on the condensation temperature).

3. Results and discussion

3.1. Preparation of the materials and photocatalytic HER performance

Water-treated C_3N_4-based materials (CN550-H, CN600-H, and CN650-H) were prepared by thermal polycondensation of a melamine precursor at 550, 600, and 650 °C, respectively, under a flow of humidified air (Fig. 1a and Table 1). To maximize the effect of water, deionized water was mixed with melamine prior to heat treatment. For comparison, CN550-A, CN600-A, and CN650-A were produced by the polycondensation of melamine without the use of water and humidified air (see SI). Fig. 1b–g and S1 show the scanning electron microscopy (SEM) and transmission electron microscopy (TEM) images of all the samples, revealing the presence of porous structures.

The visible-light active HER photocatalytic behaviors of the C_3N_4-based materials were examined using Pt and TEOA (10 vol%) as the co-catalyst and hole scavenger, respectively. As shown in Fig. 2 and Table 1, all C_3N_4-based samples exhibit photocatalytic activities for HER, and the time-normalized HER activity, which refers to the rate of H_2 evolution, varies significantly under preparation conditions such as gaseous environment and temperature (Fig. 2b). In particular, CN650-H shows the highest HER activity with an H_2 evolution rate of 157 μmol•h^{-1}•g^{-1}, which is significantly higher than those of other materials. As shown in Table S10, the activity of CN650-H is superior to those of other C_3N_4-based materials. The photocatalytic activity is preserved during the measurement up to 5 h, as the amounts of produced H_2 increase linearly with the irradiation time (Fig. 2a). To confirm the stability of the catalysts, cyclic tests were done with the most active catalysts, CN650-H and CN650-A. As shown in Fig. 2c, both materials show excellent stability as the photocatalyst for HER during consecutive four cycles. Under identical gaseous environments, materials produced at higher temperatures show higher photocatalytic activities, that is, CN650-A > CN600-A > CN550-A and CN650-H > CN600-H > CN550-H. At the same temperature, the materials produced by H_2O treatment (CN-H) show better activities than those prepared using air (CN-A), that is, CN650-H > CN650-A, CN600-H > CN600-A, and CN550-H > CN550-A. This trend in the photocatalytic HER activity suggests that both the use of humidified air and higher temperatures are beneficial for enhancing the catalytic activity for HER.

3.2. Chemical structures of C_3N_4-based materials

First, the chemical structures of the p-C_3N_4 materials were investigated using ^1H, ^{13}C, and ^{15}N cross-polarization magic-angle spinning (CP-MAS) SSNMR measurements, as shown in Fig. 3. The ^{15}N SSNMR spectra of all samples exhibit peaks at 169.7, 134.5, 113.9, and 94.4 ppm, corresponding to the C= *N*-C (N_c), *N*-C_3 (N_i), C(*N*H)C (N_b), and -*N*H_2 (N_t) groups (Fig. 3a–c), respectively [34]. The deconvoluted ^{13}C SSNMR spectra of all samples show three major peaks at 156.8, 162.6, and 165.1 ppm (Fig. 3d–f), which are attributed to the internal C atoms (C_i) in tri-*s*-triazine rings, C atoms (C_b) adjacent to bridging -NH-groups, and the combination ($C_t + C_h$) of C atoms (C_t) with terminal NH_2 and internal C atoms (C_h) adjacent to N atoms with H bonds, respectively [32]. The ^{13}C and ^{15}N SSNMR measurements confirm the formation of the tri-*s*-triazine structure. The measured X-ray photoelectron
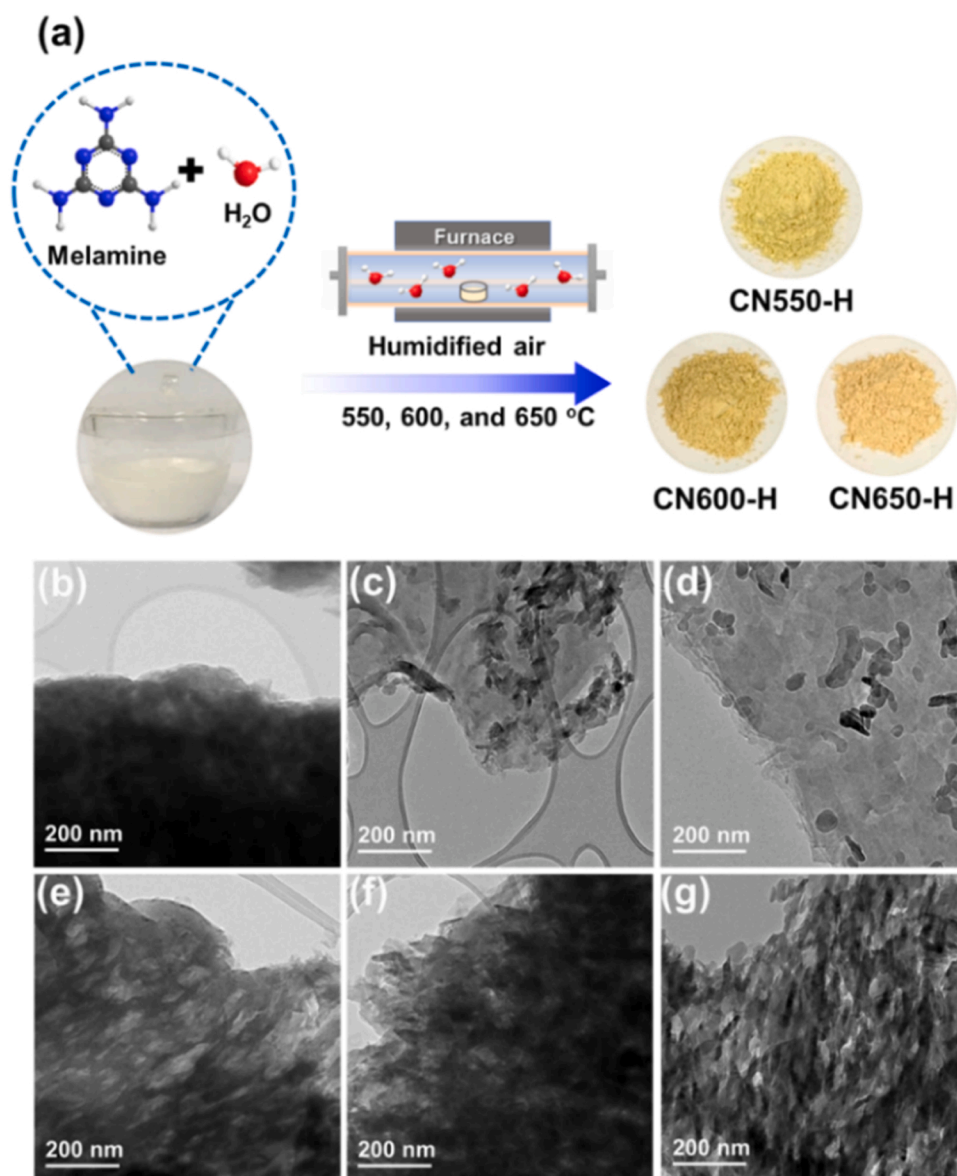
Fig. 1. (a) Scheme for the synthesis of CN550-H, CN600-H, and CN650-H. TEM images of (b) CN550-A, (c) CN600-A, (d) CN650-A, (e) CN550-H, (f) CN600-H, and (g) CN650-H.

Table 1
Synthesis conditions of all samples with their physical and photocatalytic properties.

Samples	Temp. (℃)	H_2O usage	Photocatalytic activity[a]	Surface area (m^2g^{-1})	$H_{h\text{-}t}$[b] + $H_{h\text{-}b}$[c]	C_b[d]	N- $(C)_3$/NH_x ratio[e]	Bandgap (eV)	τ_2[f]
CN550-H	550	O	51.4	16.0	69.6	11.4	2.0	2.8	3.7
CN600-H	600	O	72.4	26.5	58.5	13.3	2.6	2.9	4.5
CN650-H	650	O	157.2	39.0	48.3	17.4	6.1	2.9	6.6
CN550-A	550	X	13.5	13.1	70.3	6.2	1.0	2.7	3.5
CN600-A	600	X	28.5	21.9	64.8	10.9	1.9	2.9	3.4
CN650-A	650	X	115.7	35.2	56.1	16.6	5.7	2.9	6.2

[a] Photocatalytic activity $(\mu mol \cdot h^{-1} \cdot g^{-1})$ defined by the amount of evolved H_2 (μmol)/(amount of catalyst (g) $\cdot$ time (h)).

[b] $H_{h\text{-}t}$: H atoms for terminal $-NH_2$ groups with H bonds.

[c] $H_{h\text{-}b}$: H atoms for bridging -N*H*- groups with H bonds.

[d] C_b: C atoms adjacent to bridging -NH- groups.

[e] The ratios were calculated from the deconvoluted N 1*s* XPS spectra.

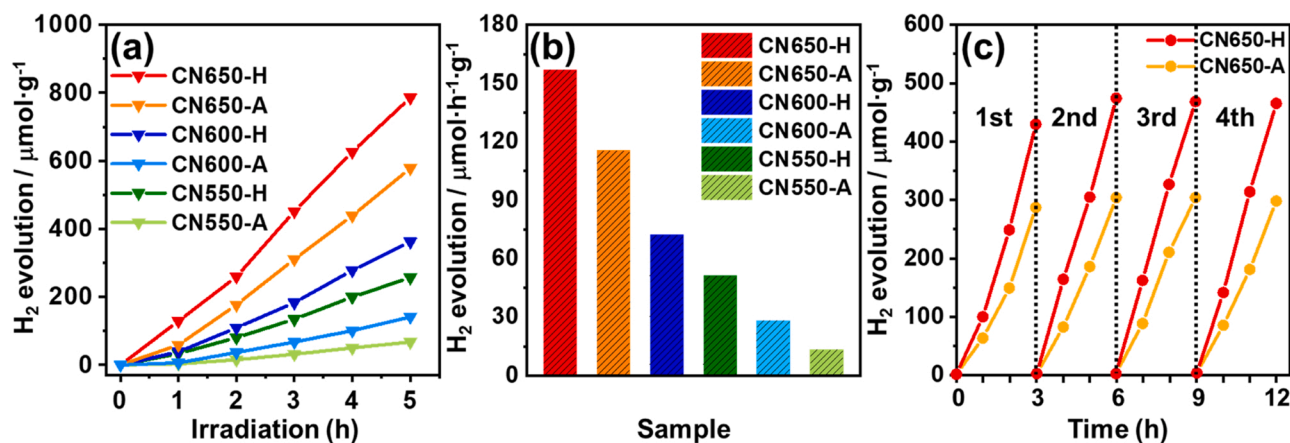[f] PL lifetimes of τ_2 calculated from the TR-PL data measured at 505 nm.

Fig. 2. (a) Photocatalytic HER activities under irradiation of visible light ($\lambda > 420$ nm) for 5 h. (b) Time-normalized HER activities measured for 5 h. (c) Cyclic tests for photocatalytic H_2 evolution of CN650-A and CN650-H.

spectroscopy (XPS) and Infrared (IR) spectra correlate with the SSNMR results and confirm the formation of tri-*s*-triazine structures (see below for further characterizations and Figs. S2–4). Based on the ^{13}C and ^{15}N SSNMR analyses and previous literature, the four peaks observed in the deconvoluted ^{1}H SSNMR spectra of all samples can be attributed to (i) bridging -N*H*- groups with (H_{h-b}) and without (H_b) H bonds and (ii) terminal -N*H*$_2$ groups with (H_{h-t}) and without (H_t) H bonds (Fig. 3g–i) [35].

To examine the effect of H_2O treatment on the chemical structure of p-C_3N_4, the SSNMR spectra of p-C_3N_4 materials produced with and without H_2O treatment are compared quantitatively. The intensities of the C_b peaks (adjacent to bridging -NH- groups) are significantly larger for the CN-H samples than for the CN-A samples (Fig. 3d–f). In addition, the N_b peaks (bridging -NH- groups) of the CN-H samples are slightly larger than those of the CN-A samples (Fig. 3a–c). These trends in the intensities of the C_b and N_b peaks indicate the formation of more bridging -NH- groups, which link two tri-*s*-triazine rings, in the CN-H samples than in the CN-A samples. More information on the H bonds can be obtained by comparing the peak intensities of the deconvoluted ^{1}H SSNMR spectra (Table S2). The amounts of protons with H bonds (H_{h-t} and H_{h-b}) are significantly larger for the CN-A samples than for the CN-H samples. Furthermore, the H_b peak intensities of the CN-H samples are larger than those of the CN-A samples. Thus, from the combination of ^{1}H, ^{13}C, and ^{15}N SSNMR data, it is revealed that p-C_3N_4 materials produced with the H_2O treatment contain fewer H bonds and more tri-*s*-triazine rings linked through amine bridges than those produced without the H_2O treatment.

We also studied the effect of polycondensation temperature on the chemical structure of p-C_3N_4. In the deconvoluted ^{13}C SSNMR spectra shown in Fig. S5, the intensity of the C_i peak remains nearly constant irrespective of the polycondensation temperature, but the intensity of the ($C_t + C_h$) peak decreases and the intensity of the C_b peak increases significantly with the increase in polycondensation temperature (Table S1). The increase in the C_b peak intensity with temperature is indicative of the formation of more bridging -NH- groups linking tri-*s*-triazine rings [32]. Meanwhile, as the polycondensation temperature increases, the peak intensity for bridging H_b clearly increases, and the peak intensities for H atoms with H bonds (H_{h-t} and H_{h-b}) decrease. The NMR data of the CN-A and CN-H samples show almost identical trends with the variation in polycondensation temperature. These results suggest that the C_3N_4 samples produced at higher temperatures contain fewer H bonds and more amine bridges.

The XPS C and N 1*s* spectra of all samples show a typical pattern for C_3N_4-based materials, revealing the formation of the C_3N_4 network (Fig. 4, S2, and S3). The deconvoluted C 1*s* spectra have peaks at 284.6, 286.2, 287.9, and 288.5 eV, which correspond to C=C/C-C, C-O, N=C-

N in tri-*s*-triazine rings, and C-NH_2 moieties, respectively (Fig. 4a and S2) [36]. In the deconvoluted N 1*s* spectra, peaks at 398.8, 400.1, and 401.4 eV are assignable to C-N=C, N-$(C)_3$, and NH_x moieties, respectively (Fig. 4b and S3) [37]. More information on the domain size can be obtained from a quantitative analysis of the deconvoluted XPS data for the selected chemical groups. The N-$(C)_3$ and -NH_x groups are located in the basal planes and at the edges of the C_3N_4 domain, respectively; therefore, the intensity ratio of the peaks corresponding to the N-$(C)_3$ and -NH_x groups in the deconvoluted N 1*s* spectra should increase when the populations of the plane and edge sites in the C_3N_4 domain are larger and smaller, respectively. Considering that a larger domain is expected to have more plane sites and fewer edge sites, the N-$(C)_3$/-NH_x intensity ratio in the XPS N 1*s* spectra can function as a measure of the average domain size, with a higher ratio indicating the presence of larger domains on average [23,38]. As shown in Table S3, the N-$(C)_3$/-NH_x intensity ratio increases with increasing polycondensation temperature. Additionally, the N-$(C)_3$/-NH_x intensity ratio is higher for CN650-H than for CN650-A. These results suggest that polycondensation at a higher temperature and with water treatment results in the generation of larger domains. When compared with the NMR data described above, the results of the XPS analysis suggest that the formation of larger C_3N_4 domains is directly associated with the formation of more -NH- bridges and fewer H bonds.

Although C_3N_4 materials that are completely condensed are not expected to exhibit an XPS peak at 284.6 eV for C=C/C-C, this peak has frequently been observed as a minor peak in previous studies [18,39], suggesting the presence of C impurities in the synthesized C_3N_4 materials. Such impurities can obstruct the transfer of photogenerated charge carriers between the C_3N_4 domains. Interestingly, in the deconvoluted XPS spectra, the intensity of the C=C/C-C peak gradually decreases with increasing polycondensation temperature for the CN-H samples but remained nearly constant for the CN-A samples irrespective of the temperature (Fig. 4a and Table S4). Such contrast of the C=C/C-C feature in the XPS spectra indicates that the C impurities are removed more completely with the H_2O treatment.

The crystal structures of the samples were determined by X-ray diffraction (XRD) measurements. Two major peaks at ~13° and ~27° are observed in all the XRD patterns and could be attributed to intralayer distances between tri-*s*-triazine rings and C_3N_4 layers, respectively (Fig. 4c and S6) [40]. Table S5 shows that as the polycondensation temperature increases, the calculated interlayer distance decreases from 3.24 Å (for CN550-H) to 3.19 Å (for CN650-H) while the full width at half maximum (FWHM) of the interlayer-distance peak decreases from 1.62° (for CN550-H) to 0.80° (for CN650-H). These results indicate that CN650-H is more densely packed along the π-stacking direction than CN550-H and CN600-H. Comparison of the XRD results for CN650-H
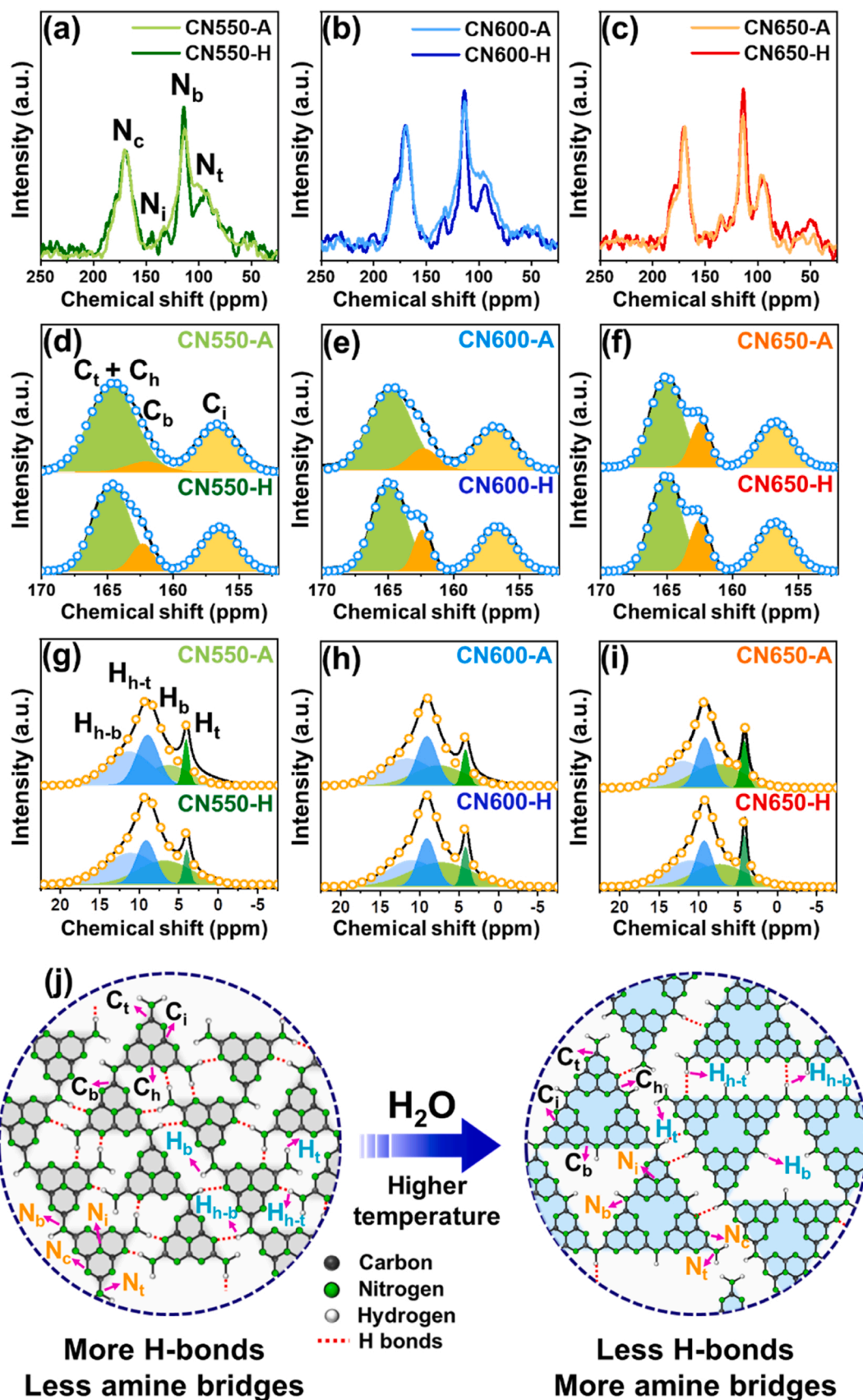
Fig. 3. CP-MAS ^{15}N SSNMR spectra of (a) CN550-A and CN550-H, (b) CN600-A and CN600-H, and (c) CN650-A and CN650-H. CP-MAS ^{13}C SSNMR spectra of (d) CN550-A and CN550-H and (e) CN600-A and CN600-H, and (f) CN650-A and CN650-H. CP-MAS ^{1}H SSNMR spectra of (g) CN550-A and CN550-H and (h) CN600-A and CN600-H, and (i) CN650-A and CN650-H. (j) Proposed chemical structures of p-C$_3$N$_4$ samples obtained from the SSNMR spectra.
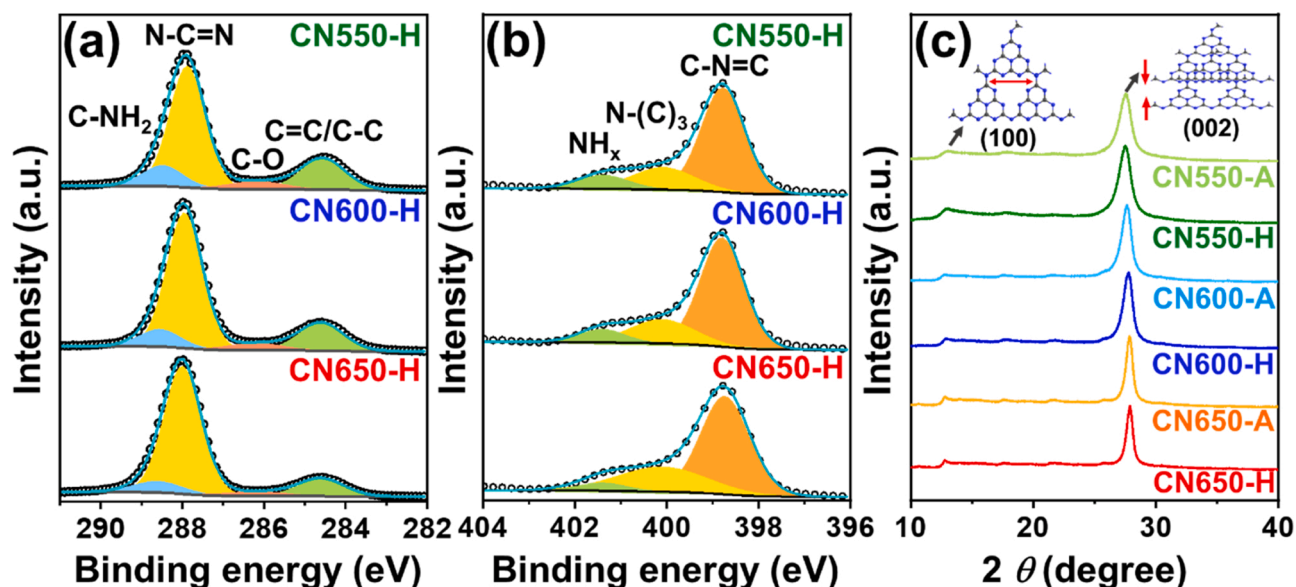
Fig. 4. Deconvoluted XPS spectra of CN550-H, CN600-H, and CN650-H; (a) C 1*s* and (b) N 1*s*. (c) XRD data of all samples.

and CN650-A reveals that both the interlayer distance and FWHM of CN650-H (3.19 Å, 0.80°) are smaller than those of CN650-A (3.21 Å, 0.86°), indicating tighter crystalline stacking in CN650-H. Additionally, the crystallite size calculated using Scherrer's equation is larger for the samples produced at higher polycondensation temperatures and with H_2O treatment [41]. Thus, based on the XRD measurements, CN650-H has a higher crystallinity than the other samples. The higher crystallinity of CN650-H can be attributed to the presence of fewer C impurities.

3.3. Quantum chemical simulation for the formation of C_3N_4-based materials

Quantum chemical simulations were performed to understand the reaction mechanism of the polycondensation of C_3N_4 under humidified gas conditions. To investigate the reaction mechanism, we needed to devise model reactant systems of a moderate size to make quantum

chemical simulations feasible without significant loss of simulation accuracy. Considering that melems are transformed to melemOH in hydrolysis conditions [42,43], as representative model reactant systems, we used (i) melem, which is a tri-*s*-triazine derivative with three amino groups, and (ii) melemOH, where one of the amino groups of melem is replaced by a hydroxyl group.

Fig. 5 shows the potential energy curves for the formation of dimelem via two different reaction pathways: (i) a common C_3N_4 formation pathway starting from two melems (melem + melem), and (ii) a relevant pathway for this work, starting from one melem and one melemOH (melem + melemOH). To facilitate discussion of the melem + melem pathway, we label two melems, melem-A and melem-B, to distinguish them from each other. When the two melems are in close proximity, the amino group of melem-A attacks the carbon atom attached to an amino group in melem-B. Interestingly, the C-N bond formation between the two melems is accompanied by the transfer of H atoms in melem-A to the amino group attached to the carbon atom, which participates in C-N
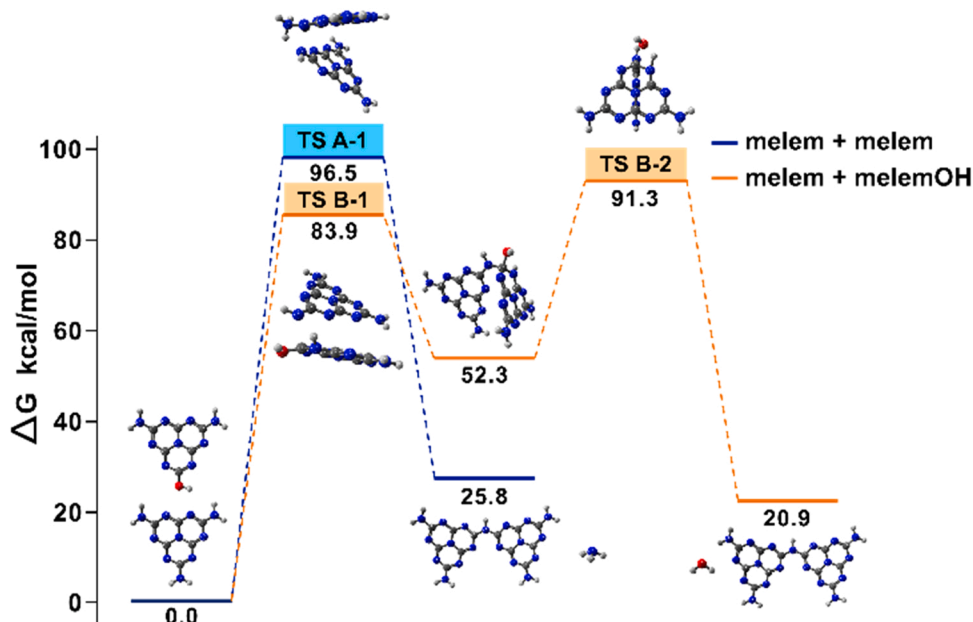

Fig. 5. Potential energy curves for dimelem formation via two different reaction pathways. The reaction pathways starting from either melem + melem (blue line) or melem + melemOH (orange line) were considered. Chemical structures of reactants, transition states, intermediates, and products are shown with the ball-and-stick model employing carbon (black), oxygen (red), nitrogen (blue), hydrogen (white) atoms. For each chemical species, the Gibbs free energy is given in the unit of kcal/mol. (For interpretation of the references to color in this figure, the reader is referred to the web version of this article.)

bond formation in melem-B. The structure of the transition state and the corresponding vibrational normal mode (TS A-1) for the melem + melem pathway indicates a single-step, concerted mechanism for C-N bond formation and H-atom transfer (see Fig. S7 for the graphical description of the normal mode). Subsequently, ammonia is spontaneously released. The final products of the melem + melem pathway are dimelem and free ammonia, and this reaction pathway is predicted to be thermodynamically uphill by 25.8 kcal/mol.

As a model system for the reaction in a humidified gas environment, we considered the reaction between the carbon with a hydroxyl group in melemOH and the carbon with an amino group in melem. Remarkably, when an amino group in melem is replaced with a hydroxyl group, the reaction mechanism (and energetics) changes dramatically from a single-step, concerted mechanism to a two-step, sequential mechanism. In the first step of the melem + melemOH pathway, the nitrogen atom of an amino group in melem attacks the carbon atom with a hydroxyl group in melemOH to form a C-N bond, while one hydrogen atom from the amino group is concomitantly transferred to the nitrogen atom of the adjacent *s*-triazine six-membered ring in melemOH. The structure of the transition state (TS B-1) is graphically described in Fig. 5, and it can be seen that the reaction barrier of the melem + melemOH pathway is smaller than that of the melem + melem pathway by 12.6 kcal/mol. The second step of the melem + melemOH pathway is the formation and release of water. Quantum chemical simulations reveal that this process occurs via the detachment of the OH group and the H atom transferred in the previous step and requires much less activation energy than the first step (see TS B-2). The final products of the melem + melemOH pathway are dimelem and water, and this reaction pathway is thermodynamically unfavorable by 20.9 kcal/mol. While both pathways are predicted to be thermodynamically unfavorable, the relative heights, rather than the actual values, of the activation barriers of the two pathways are a key factor in determining the reaction pathway. Since the dimelem formation from melem and melemOH requires less activation energy by 12.6 kcal/mol and produces more stable products (by 4.9 kcal/mol) than the dimelem formation from two melems, we can conclude that the melem + melemOH pathway is a more relevant mechanism for the dimelem formation in the humidified gas environment.
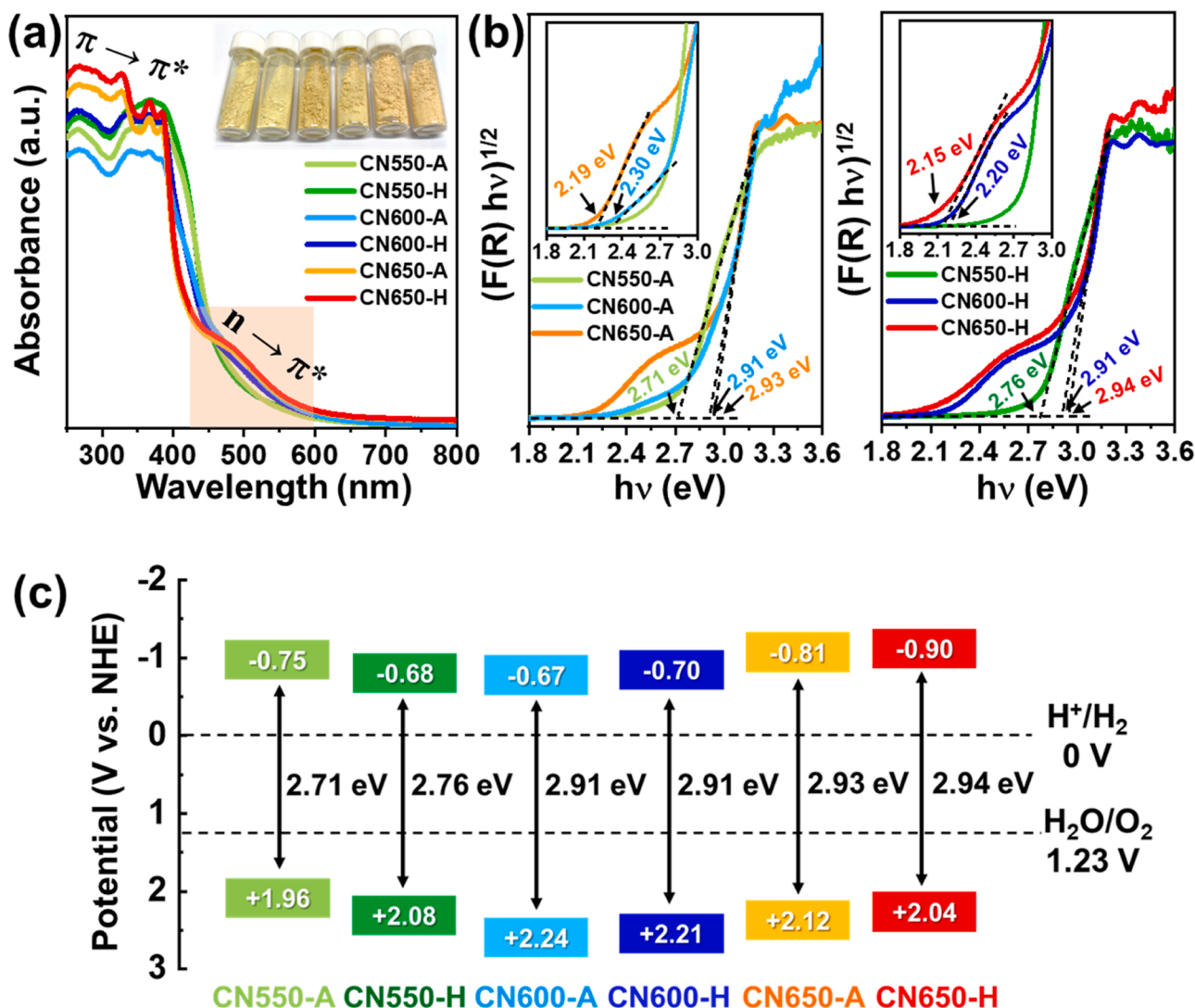

Fig. 6. (a) Absorption spectra of CN550-A (light green), CN600-A (light blue), CN650-A (orange), CN550-H (green), CN600-H (blue), and CN650-H (red). Inset: photographs of CN550-A, CN550-H, CN600-A, CN600-H, CN650-A, and CN650-H, in order, from left to right. (b) Kubelka–Munk plots of diffuse reflectance spectra. (Left) CN550-A (light green), CN600-A (light blue), and CN650-A (orange). (Right) CN550-H (green), CN600-H (blue), and CN650-H (red). Inset: enlarged graphs in a selected spectral region. (c) Band structure diagrams for all the samples. (For interpretation of the references to color in this figure, the reader is referred to the web version of this article.)

3.4. Photophysical properties of C₃N₄-based materials

To understand the photocatalytic properties of the C_3N_4 materials, we performed spectroscopic measurements including absorption spectra, 2D EEM spectra (which can provide static photoluminescence (PL) spectra and PL excitation (PLE)), and TR-PL decays, as shown in Figs. 6–8, S10, and S11. In the absorption spectra shown in Fig. 6a, spectral features with large intensities are observed at wavelengths smaller than 400 nm, and these features can be assigned to the $\pi \rightarrow \pi*$ transition and transitions to higher electronic states than the bandgap [37]. In addition, an absorption feature centered at 485 nm is observed and could be assigned to the $n \rightarrow \pi*$ transition or a transition to other mid-gap states associated with atomic/structural defects in p-C_3N_4 [44,45]. Notably, the 485 nm feature is more pronounced in the absorption spectra of the CN650-H and CN650-A samples, probably due to the structural distortion of the p-C_3N_4 layers in the samples prepared at 650 °C, thereby breaking the symmetry and allowing the occurrence of the forbidden mid-gap transition [46]. In addition, we note that a broad absorption feature at 400–430 nm significantly decreased with

the increase in polycondensation temperature and is completely absent in the CN650-H sample, as shown in the absorption (Fig. 6a) and deconvoluted (Fig. S8) spectra. According to the ^{13}C and ^1H SSNMR analysis described in the previous section, the CN650-H sample contains a significantly lower amount of H bonds than the CN550-H and CN600-H samples. Therefore, the 415 nm absorption feature must be associated with the C_3N_4 network linked by the H bonds.

As shown in Fig. 6b, the bandgaps of all p-C_3N_4 materials were calculated with the Kubelka–Munk function from the diffuse reflectance spectra (DRS) and determined to be 2.71, 2.76, 2.91, 2.91, 2.93, and 2.94 eV for CN550-A, CN550-H, CN600-A, CN600-H, CN650-A, and CN650-H, respectively. The bandgaps of the p-C_3N_4 materials indicate that all the p-C_3N_4 materials investigated in this work have bandgaps of suitable energies to absorb visible light. In addition, as shown in Fig. S9, Mott–Schottky plots were used to determine the conduction band (CB) positions. The derived flat-band potentials of CN550-A, CN550-H, CN600-A, CN600-H, CN650-A, and CN650-H were determined to be -0.75, -0.68, -0.67, -0.81, -0.91, and -0.90 V (vs. the normal hydrogen electrode, NHE), respectively, indicating that the CBs of all the
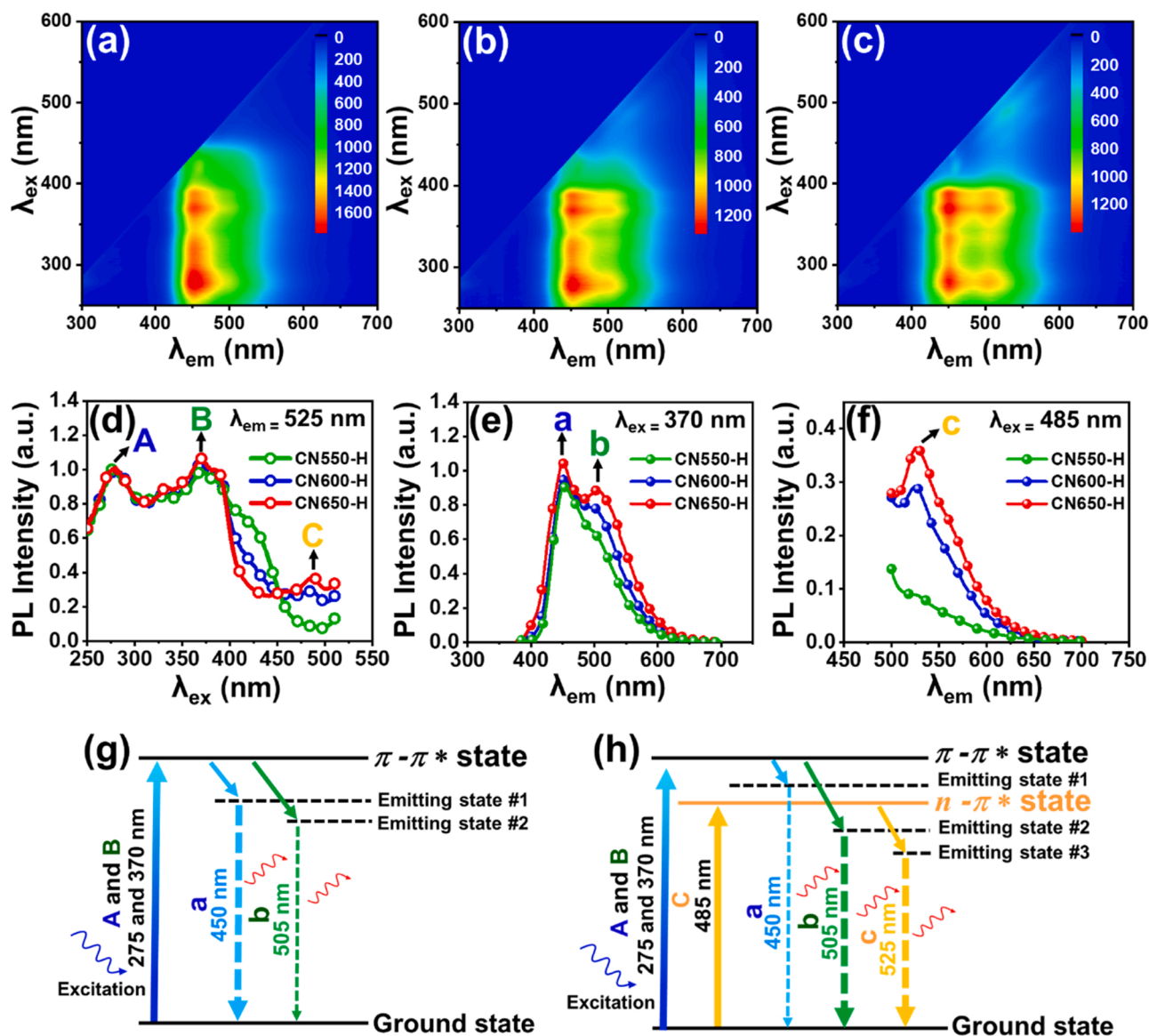

Fig. 7. 2D EEM spectra of (a) CN550-H, (b) CN600-H, and (c) CN650-H. (d) Normalized PLE spectra of CN550-H, CN600-H, and CN650-H measured at 525 nm emission wavelength. Normalized PL spectra of CN550-H, CN600-H, and CN650-H measured with excitation at (e) 370 nm and (f) 485 nm. Proposed energy level diagrams of (g) CN550-H and (h) CN650-H.
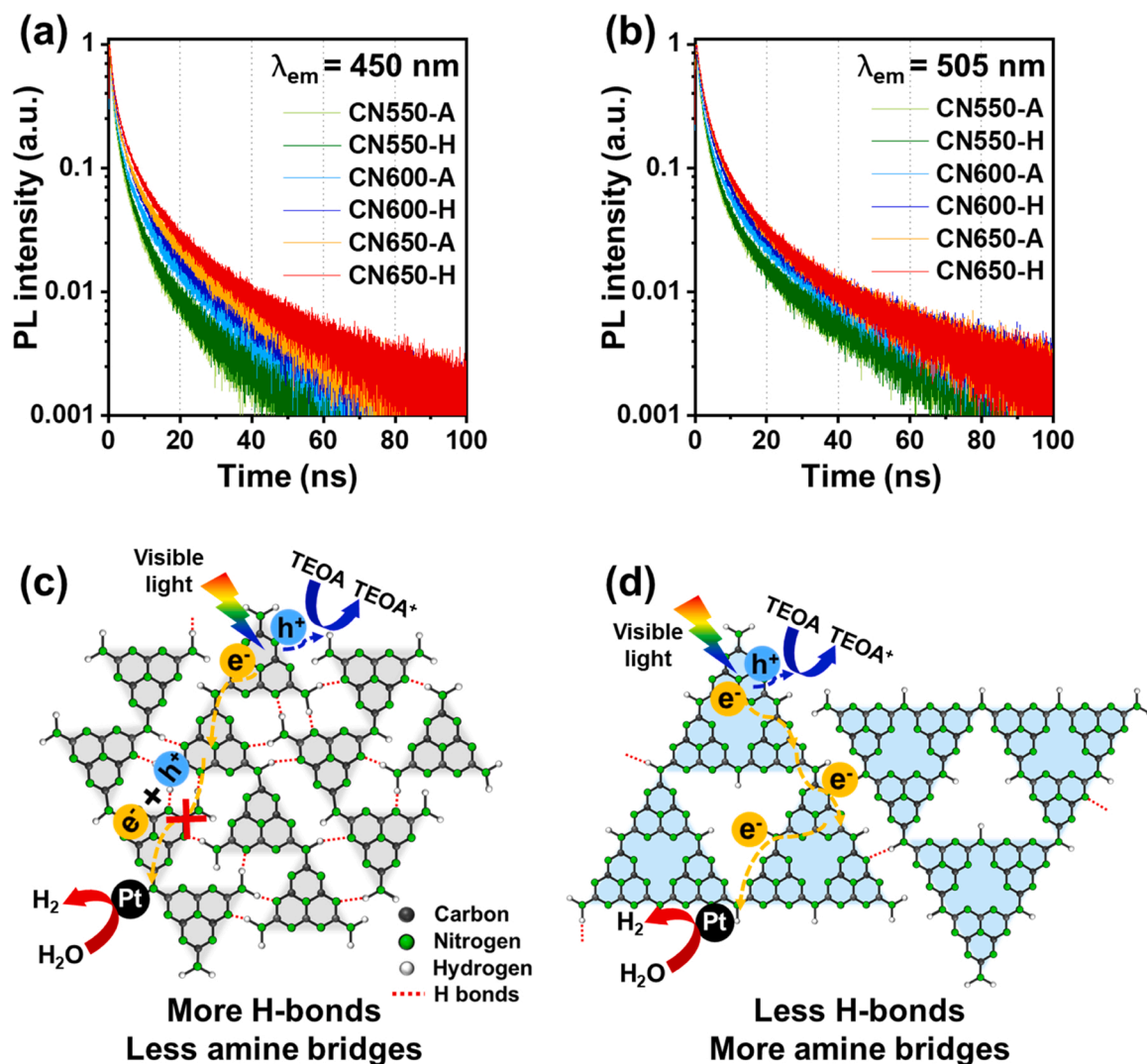
Fig. 8. Time-resolved PL decays measured with 393 nm excitation at the emission wavelengths of (a) 450 nm and (b) 505 nm. Schematic of intraplanar exciton migration in (c) CN550-H and (d) CN650-H.

samples are located at lower energies than the H_2 evolution potential. Therefore, all samples investigated in this work have CBs and bandgaps of suitable energies for visible-light redox catalysts for H_2 production. In the inset of Fig. 6b, the transition energy from the VB to a mid-gap orbital (i.e., sub-bandgap) was calculated for CN600-A, CN600-H, CN650-A, and CN650-H [47–49], while the sub-bandgap could not be determined for CN550-A and CN550-H because of the absence of shoulder peaks in their spectra. Based on the calculated sub-bandgaps, when electrons are excited from the VB edge to a mid-gap orbital, the excited electrons possess suitable potentials for HER to occur (Fig. S10). Therefore, the excitation to the mid-gap orbital or CB for CN600-A, CN600-H, CN650-A, and CN650-H can be utilized to reduce H^+ to H_2. In contrast, for CN550-A and CN550-H, only excitation to the CB can be used for the HER.

The 2D EEM spectra were measured for all powder samples, as shown in Fig. 7a–c and S11. The 2D EEM spectrum maps the correlation between the excitation and emission features in a 2D spectrum. From the 2D EEM spectra, the PLE spectrum can be extracted to examine the absorption features contributing to a specific emission feature. For example, in the PLE spectra at an emission wavelength of 525 nm (Fig. 7d), we observe the same spectral features as those observed in the absorption spectra in Fig. 6a. The peaks at 275 nm (absorption feature **A** in Fig. 7d) and 370 nm (absorption feature **B**) are commonly observed in

the 2D EEM spectra for all the samples and can be attributed to the transition to highly excited states and the $\pi \rightarrow \pi *$ transition, respectively. The broad spectral feature at 400–430 nm decreases with an increase in polycondensation temperature and can be assigned to the C_3N_4 network linked by H bonds, as supported by the ^{13}C SSNMR, ^{1}H SSNMR, N 1*s* XPS, and absorption spectra (Tables S1–S3, and Fig. S8). Finally, the feature at 485 nm (absorption feature **C**) is observed at an emission wavelength of 525 nm, which is more pronounced for the CN650-H and CN650-A samples. Feature **C** can be assigned to the $n \rightarrow \pi *$ transition or a transition to other mid-gap defect states.

From the 2D EEM spectra, the PL spectrum can also be extracted to examine the emission features associated with a specific absorption feature. In the PL emission spectra at an excitation wavelength of 370 nm (Fig. 7e) extracted from the 2D EEM spectra, two major peaks are observed at 450 nm (emission feature **a**) and 505 nm (emission feature **b**) emission wavelengths. The peak at 450 nm stays nearly constant irrespective of the polycondensation temperature, whereas the peak at 505 nm grows up significantly with the increase in polycondensation temperature. Considering that both 450 nm and 505 nm peaks are observed with the excitation at 275 nm (absorption feature **A**) and 370 nm (absorption feature **B**), as shown in the 2D EEM spectra in Fig. 7a–c, both emission features **a** and **b** must be associated with the $\pi \rightarrow \pi *$ transition and/or the transition to highly excited states, while the

emission feature **b** at 505 nm seems to more sensitively reflect the structural features of samples prepared at higher temperatures, for example, higher crystallinity and larger domain size. In the PL emission spectra measured at an excitation wavelength of 485 nm (Fig. 7f), a new emission feature is observed at 525 nm (emission feature **c**). Notably, the emission feature **c** increases substantially with the increase in polycondensation temperature. Since the excitation at 485 nm, which coincides with absorption feature **C**, selectively gives rise to the emission feature **c**, it must be directly associated with the absorption feature **C**, which corresponds to the transition to mid-gap states. The strong correlation between the features **c** and **C** is further confirmed by the growth of the 525 nm emission feature with the increase in polycondensation temperature, which correlates with the temperature dependence of the absorption feature **C**. Therefore, both features **c** and **C** must be associated with the n → π * transition. In particular, the growth of the emission feature **c** with the increase in polycondensation temperature must be associated with the structural distortion of the p-C_3N_4 network, particularly the amine bridges linking tri-*s*-triazine groups, which become more prevalent in the p-C_3N_4 network of CN650-H. According to a previous theoretical study, because of the closely spaced lone pair electrons of N atoms at the *ortho* positions between two neighboring of tri-*s*-triazine rings, the amine bridges cause structural distortion of the C_3N_4 network, which can induce the occurrence of the forbidden n → π * transition [48]. This could be an origin for the mid-gap states of CN650-H. In addition, possible defect sites in the C_3N_4 network might be another reason inducing the mid-gap states.

By combining the results of the absorption and emission spectra, we propose energy level diagrams for the absorption and emission states of CN550-H and CN650-H in Fig. 7g and h, respectively. In CN550-H (see Fig. 7g), the π → π * state and highly excited states are generated by photoexcitation at 275 nm and 370 nm, respectively, and subsequently relax non-radiatively into emitting states #1 and #2, which are associated with the emission at 450 and 505 nm, respectively. In contrast, in CN650-H (see Fig. 7h), the n → π * state is also generated by photoexcitation at 485 nm and relaxes into an extra emitting state (emitting state #3), which is associated with the emission at 525 nm.

To investigate the dynamics of the excited states of the p-C_3N_4 samples in association with the photocatalytic activity, we performed TR-PL measurements at three emission wavelengths, 450, 505, and 525 nm, which correspond to major emission peaks in the PL spectrum (Fig. 8a – b and S12). The TR-PL decays were fitted by three exponential functions and their individual time constants, τ_1, τ_2, and τ_3, in increasing order, which can be assigned to exciton recombination, intralayer exciton migration, and interlayer exciton migration, respectively [50, 51]. In Tables S6–S8, the time constants, τ_1, τ_2, and τ_3 are listed for the three emission wavelengths. In general, excitons bound to intrinsic defect states tend to recombine more slowly than free excitons. When comparing the time constants of the TR-PL decays at the three emission wavelengths, we infer that the 450 nm emission feature is of a free-excitonic character, and the 505 nm and 525 nm emission features are of a bound-exciton character [50]. At all three emission wavelengths, τ_1, τ_2, and τ_3 increase with the polycondensation temperature, except that the increase in τ_3 was saturated for the samples prepared at 600 °C (that is, CN600-A and CN600-H). In addition, the CN-H samples exhibit slower PL decay than the CN-A samples. In particular, the CN650-H sample exhibits the slowest overall TR-PL decay among all the samples; in particular, it has the longest τ_2, which corresponds to the time taken for intralayer exciton migration. This result of the TR-PL measurement can be interpreted in combination with the results of structural analysis and the existence of the mid-gap states. In the ^{13}C and ^{15}N SSNMR spectra (Fig. 3a–f), CN650-H exhibits stronger peaks corresponding to amine bridging groups than the other samples, indicating that the bridging structure of CN650-H serves as an efficient pathway for the intralayer migration of excitons and charge carriers. Furthermore, the presence of mid-gap states in CN650-H prolongs the lifetimes of the excited states by diminishing electron-hole recombination. As a result,

CN650-H exhibits the most efficient photocatalytic activity among all C_3N_4 materials investigated in this study.

Based on all the experimental results described above, we can explain the difference in the intraplanar exciton migration associated with photocatalytic H_2 generation in CN550-H and CN650-H (Fig. 8c – d). Under visible-light irradiation, excitons are generated in CN550-H and CN650-H and are subsequently separated into electrons and holes. As shown in Fig. 8c, H-bonds between tri-*s*-triazine rings are abundant in CN550-H. As a result, the photogenerated electrons are localized within each melon strand and their intralayer migration is obstructed, leading to easier recombination of photogenerated charge carriers. In contrast, as shown in Fig. 8d, there exist fewer hydrogen bonds and more amine bridges in CN650-H than in CN550-H. As a result, tri-*s*-triazine rings form a lattice with higher long-range order, facilitating more facile migration of photogenerated electrons towards the Pt co-catalyst. Consequently, the electrons transferred to the Pt co-catalyst are consumed to reduce H_2O or H^+ to produce H_2, and the remaining holes are removed by oxidizing a sacrificial reagent, TEOA.

3.5. Electrophysical properties of C_3N_4-based materials and size distribution of Pt nanoparticles

The surface area and pore size of C_3N_4 materials are important factors that determine their catalytic performance. The Brunauer–Emmett–Teller (BET) surface area increases with the polycondensation temperature, and CN650-H has the highest BET surface area of 39.0 m^2g^{-1}. The N_2 adsorption-desorption isotherm curves of all the samples are type IV with H3 hysteresis loops (Fig. S13). This result reveals that these materials contain mesopores with slit-shaped pores, which are derived from the aggregation of plate-like particles [52]. The Barrett–Joyner–Halenda (BJH) pore size distributions show that all samples have similar pore diameters in the range of 2–3 nm (Fig. S14). Thermogravimetric analysis (TGA) measurements confirm that all the samples are stable up to 500 °C but decomposed completely at ~700 °C (Fig. S15). The thermal stability of the materials increases as the polycondensation temperature increases. At identical polycondensation temperatures, the CN-H samples show slightly higher thermal stability than the CN-A samples (Table S9), which can be attributed to the higher crystallinity and larger domain size of the CN-H samples.

The photocurrent responses of the C_3N_4 materials were measured using sequential on-off visible light irradiation. As shown in Fig. 9a, the generated photocurrent increases with the polycondensation temperature and the application of H_2O treatment. As a result, CN650-H generates a much higher current density than other materials, which means that the facile separation of photogenerated electron/hole pairs predominantly occurs in CN650-H, rather than electron-hole recombination. This photocurrent measurement result correlates with the TR-PL result, revealing the longest lifetime of charge carriers in CN650-H. Based on the Nyquist plots of the measured electrochemical impedance spectroscopy (EIS) data shown in Fig. 9b, CN650-H possesses the lowest charge transfer resistance (R_{ct}), which indicates that CN650-H has efficient charge transfer properties at the interfaces. In agreement with the trend of the photocurrent response, materials produced at higher temperatures and with H_2O treatment exhibit more efficient interfacial charge transfer. The higher photocurrent and lower interfacial resistance of CN650-H, which may result from its better crystallinity, supports the superiority of CN650-H as a photocatalyst.

Pt nanoparticles deposited on the surface of the materials (see Experimental section) were used as co-catalysts for photocatalytic HER. Because photoexcited charge carriers transfer through the Pt particles, their uniform dispersion and narrow size distribution can be critical factors for determining the photocatalytic performance [30,53]. The TEM images of the Pt-deposited samples show that Pt particles are well dispersed at the surfaces (Fig. S16). The average size and size distribution of the Pt particles were determined from TEM images. Among all the
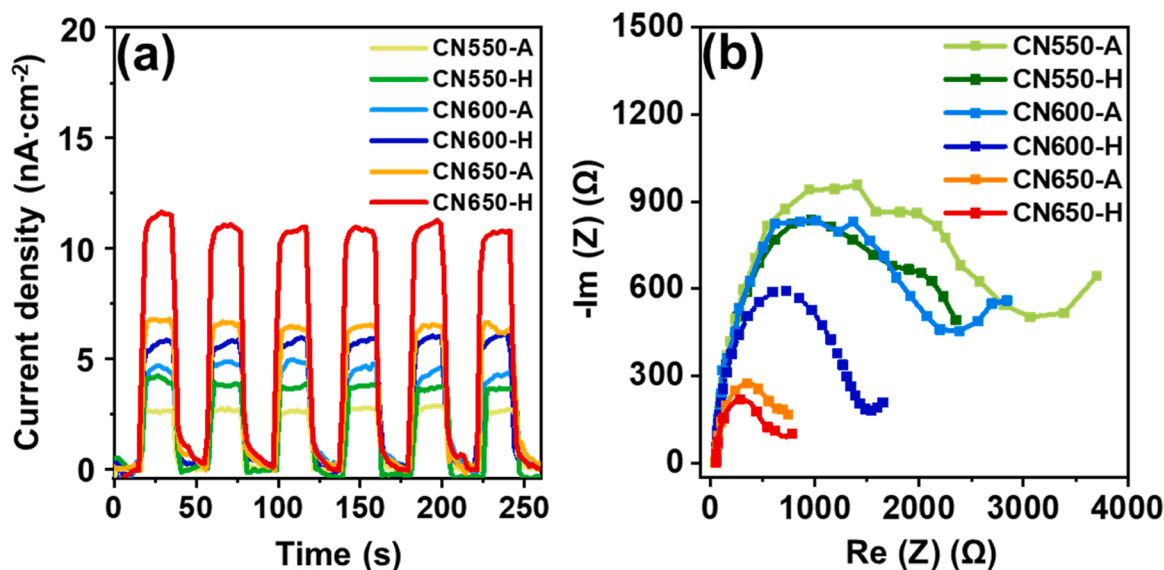
Fig. 9. (a) Photocurrent responses of all the samples under sequential on-off visible light irradiation. (b) Nyquist plots of the measured EIS data for all the samples.

samples, CN650-H contains the Pt particles with the smallest average size (12.0 nm) and the narrowest size distribution ($\pm$ 3.3 nm). Both factors decrease as the polycondensation temperature increased. At the same polycondensation temperature, the CN-H samples contain smaller particles with narrower size distributions than the CN-A samples. This uniform dispersion of small Pt particles in CN650-H is beneficial for achieving efficient charge carrier transfer during photocatalytic reactions.

3.6. Relationship between chemical structure and photocatalytic properties

In the previous sections, we characterized the chemical structures and photophysical properties of p-C_3N_4 materials as well as their photocatalytic properties for the HER, as summarized in Table 1. In particular, we demonstrated that the photocatalytic activity of p-C_3N_4 materials varies significantly depending on the treatment with H_2O and the polycondensation temperature. Specifically, the CN-H samples show much higher catalytic activities than the CN-A samples, and the photocatalytic activity increases significantly with an increase in the polycondensation temperature. In this section, we provide further insight into the relationship between the photocatalytic behavior and chemical structure of the p-C_3N_4 materials.

Based on the intensive XRD and various spectroscopic characterizations, it was revealed that H_2O treatment during the formation of p-C_3N_4 materials leads to the formation of more amine bridges and fewer H bonds. Such structural changes in p-C_3N_4 materials are also induced by the increase in polycondensation temperature, regardless of the H_2O treatment. The resultant H_2O-treated materials (CN-Hs) contain larger intralayer domains and higher crystallinity than the materials prepared without H_2O treatment (CN-As).

Photophysical characterizations revealed that all the CN-H and CN-A samples have band structures, such as CB edge energies and bandgaps, which are suitable for catalyzing HER using visible light. In particular, CN650-H exhibits the slowest overall TR-PL decay and the longest τ_2, which corresponds to intralayer exciton migration. This result indicates that photoexcited charge carriers flow more efficiently along the C_3N_4 network in CN650-H, owing to the better intralayer ordering of tri-*s*-triazine structures through amine bridges. The mid-gap states present in CN650-H not only improve the absorption of visible light by expanding the absorption bandwidth but also serve as trap sites for photogenerated charge carriers, thus suppressing the recombination of electrons and

holes. Thus, chemical modification achieved by temperature control and H_2O treatment would result in a more efficient transfer of the photogenerated charge carriers to the catalytic HER. Accordingly, CN650-H generates a higher photocurrent under visible light irradiation and possesses a lower resistance at the interfaces, presumably due to its better crystallinity. Furthermore, as shown in Fig. S13, the catalytic activities of CN materials increase with BET specific surface areas. Based on the combination of all these findings from the comprehensive characterizations performed in this work, it was revealed how the structural changes associated with H bonds and amine bridges in the C_3N_4 network affect the photocatalytic HER performance. During the synthetic processes, H bonds between C_3N_4 domains are broken and the domains are linked thorough amine bridges. The resulting p-C_3N_4 materials contain the better crystallinity, leading the facile transfer of photo-generated charge carriers along the network. With the combination of suitable band structures such as the band gaps for visible light and the reduction potential for HER, the materials show improved photocatalytic HER performance under visible light irradiation.

4. Conclusions

In this study, we developed a novel water-assisted route to produce p-C_3N_4 materials containing more amine bridges and fewer H bonds. The CN-H samples were produced by the polycondensation of melamine using water and humidified air at various temperatures (550, 600, and 650 °C), and the CN-A samples were prepared without the use of water as a reference. CN650-H shows the highest photocatalytic HER activity of 157.2 μmol$\cdot$h$^{-1}\cdot$g^{-1} under visible light irradiation. From comprehensive experimental and theoretical studies, we elucidated the relationship between the photocatalytic activity, chemical structure, and photophysical properties of the p-C_3N_4 materials. This study opens new avenues for controlling the photophysical properties of C_3N_4 materials. Furthermore, we believe that our new reaction route using H_2O treatment will be useful for producing efficient metal-free photocatalysts to generate H_2 using visible light.

CRediT authorship contribution statement

Dawoon Jang: Conceptualization, Investigation, Validation, Formal analysis, Writing – original draft. **Seungjoo Choi**: Investigation, Formal analysis. **Nam Hee Kwon**: Investigation, Formal analysis. **Kyung Yeon Jang**: Investigation, Formal analysis. **Suyeon Lee**: Investigation. **Tae-**

Woo Lee: Writing – review & editing. **Seong-Ju Hwang**: Writing – review & editing, Funding acquisition. **Hyungjun Kim**: Software, Data Curation, Writing – original draft, Writing – review & editing. **Jeongho Kim**: Writing – review & editing, Funding acquisition, Supervision. **Sungjin Park**: Conceptualization, Writing – review & editing, Funding acquisition, Supervision, Project administration.

Declaration of Competing Interest

The authors declare that they have no known competing financial interests or personal relationships that could have appeared to influence the work reported in this paper.

Acknowledgements

Appendix A. Supporting information

Supplementary data associated with this article can be found in the online version at doi:10.1016/j.apcatb.2022.121313.

References

[1] F.K. Kessler, Y. Zheng, D. Schwarz, C. Merschjann, W. Schnick, X. Wang, M. J. Bojdys, Functional carbon nitride materials—design strategies for electrochemical devices, Nat. Rev. Mater. 2 (2017) 1–17.

[2] P. Audebert, E. Kroke, C. Posern, S.-H. Lee, State of the art in the preparation and properties of molecular monomeric *s*-heptazines: syntheses, characteristics, and functional applications, Chem. Rev. 121 (2021) 2515–2544.

[3] L. Lin, Z. Lin, J. Zhang, X. Cai, W. Lin, Z. Yu, X. Wang, Molecular-level insights on the reactive facet of carbon nitride single crystals photocatalysing overall water splitting, Nat. Catal. 3 (2020) 649–655.

[4] G. Zhang, M. Liu, T. Heil, S. Zafeiratos, A. Savateev, M. Antonietti, X. Wang, Electron deficient monomers that optimize nucleation and enhance the photocatalytic redox activity of carbon nitrides, Angew. Chem. Int. Ed. 58 (2019) 14950–14954.

[5] G. Zhang, G. Li, T. Heil, S. Zafeiratos, F. Lai, A. Savateev, M. Antonietti, X. Wang, Tailoring the grain boundary chemistry of polymeric carbon nitride for enhanced solar hydrogen production and CO_2 reduction, Angew. Chem. Int. Ed. 58 (2019) 3433–3437.

[6] P. Kumar, E. Vahidzadeh, U.K. Thakur, P. Kar, K.M. Alam, A. Goswami, N. Mahdi, K. Cui, G.M. Bernard, V.K. Michaelis, C_3N_5: a low bandgap semiconductor containing an azo-linked carbon nitride framework for photocatalytic, photovoltaic and adsorbent applications, J. Am. Chem. Soc. 141 (2019) 5415–5436.

[7] C. Huang, Y. Wen, J. Ma, D. Dong, Y. Shen, S. Liu, H. Ma, Y. Zhang, Unraveling fundamental active units in carbon nitride for photocatalytic oxidation reactions, Nat. Commun. 12 (2021) 1–8.

[8] A. Kumar, P. Raizada, A. Hosseini-Bandegharaei, V.K. Thakur, V.-H. Nguyen, P. Singh, C-, N-Vacancy defect engineered polymeric carbon nitride towards photocatalysis: viewpoints and challenges, J. Mater. Chem. A 9 (2021) 111–153.

[9] A.J. Rieth, Y. Qin, B.C. Martindale, D.G. Nocera, Long-lived triplet excited state in a heterogeneous modified carbon nitride photocatalyst, J. Am. Chem. Soc. 143 (2021) 4646–4652.

[10] S. Wu, H. Yu, S. Chen, X. Quan, Enhanced photocatalytic H_2O_2 production over carbon nitride by doping and defect engineering, ACS Catal. 10 (2020) 14380–14389.

[11] Y. Zheng, Y. Chen, B. Gao, B. Lin, X. Wang, Black phosphorus and carbon nitride hybrid photocatalysts for photoredox reactions, Adv. Funct. Mater. 30 (2020), 2002021.

[12] S. Park, Y.-H. Kim, S. Kang, D. Lim, J. Park, D. Jang, S. Choi, J. Kim, S. Han, T.-W. Lee, Production of C, N alternating 2D materials using covalent modification and their electroluminescence performance, Small Sci. 1 (2021), 2000042.

[13] H.Y. Hoh, Y. Zhang, Y.L. Zhong, Q. Bao, Harnessing the potential of graphitic carbon nitride for optoelectronic applications, Adv. Opt. Mater. (2021), 2100146.

[14] D. Jang, H. Ahn, J. Oh, D. Lim, C.H. Kim, S. Choi, Y.H. Kim, J. Park, K.Y. Jang, R. J. Yoo, Production of metal-free C, N alternating nanoplatelets and their In Vivo fluorescence imaging performance without labeling, Adv. Funct. Mater. 30 (2020), 2004800.

[15] K. Xiao, B. Tu, L. Chen, T. Heil, L. Wen, L. Jiang, M. Antonietti, Photo-driven ion transport for a photodetector based on an asymmetric carbon nitride nanotube membrane, Angew. Chem. Int. Ed. 58 (2019) 12574–12579.

[16] A. Wang, C. Wang, L. Fu, W. Wong-Ng, Y. Lan, Recent advances of graphitic carbon nitride-based structures and applications in catalyst, sensing, imaging, and LEDs, Nanomicro Lett. 9 (2017) 1–21.

[17] H. Basharnavaz, A. Habibi-Yangjeh, M. Pirhashemi, Graphitic carbon nitride as a fascinating adsorbent for toxic gases: a mini-review, Chem. Phys. Lett. 754 (2020), 137676.

[18] H. Kim, D. Lim, N.H. Kwon, S. Son, S. Choi, J. Kim, S.-J. Hwang, S. Park, Dramatic change of morphological, photophysical, and photocatalytic H_2 evolution properties of C_3N_4 materials by the removal of carbon impurities, ACS Appl. Energy Mater. 3 (2020) 4812–4820.

[19] S. Seok, M. Choi, Y. Lee, D. Jang, Y. Shin, Y.-H. Kim, C. Jo, S. Park, Ni nanoparticles on Ni core/N-doped carbon shell heterostructures for electrocatalytic oxygen evolution, ACS Appl. Nano Mater. 4 (2021) 9418–9429.

[20] G. Zhang, M. Liu, T. Heil, S. Zafeiratos, A. Savateev, M. Antonietti, X. Wang, Electron deficient monomers that optimize nucleation and enhance the photocatalytic redox activity of carbon nitrides, Angew. Chem. Int. Ed. 131 (2019) 15092–15096.

[21] G. Wang, T. Zhang, W. Yu, R. Si, Y. Liu, Z. Zhao, Modulating location of single copper atoms in polymeric carbon nitride for enhanced photoredox catalysis, ACS Catal. 10 (2020) 5715–5722.

[22] D. Zhu, Q. Zhou, Novel Bi_2WO_6 modified by N-doped graphitic carbon nitride photocatalyst for efficient photocatalytic degradation of phenol under visible light, Appl. Catal. B Environ. 268 (2020), 118426.

[23] J. Oh, J.M. Lee, Y. Yoo, J. Kim, S.-J. Hwang, S. Park, New insight of the photocatalytic behaviors of graphitic carbon nitrides for hydrogen evolution and their associations with grain size, porosity, and photophysical properties, Appl. Catal. B Environ. 218 (2017) 349–358.

[24] Q. Cao, B. Kumru, M. Antonietti, B.V. Schmidt, Graphitic carbon nitride and polymers: a mutual combination for advanced properties, Mater. Horiz. 7 (2020) 762–786.

[25] B. Kumru, M. Antonietti, B.V. Schmidt, Enhanced dispersibility of graphitic carbon nitride particles in aqueous and organic media via a one-pot grafting approach, Langmuir 33 (2017) 9897–9906.

[26] Z. Wang, B. Jin, J. Peng, W. Su, K. Zhang, X. Hu, G. Wang, J.H. Park, Engineered polymeric carbon nitride additive for energy storage materials: a review, Adv. Funct. Mater. 31 (2021), 2102300.

[27] Y. Li, F. Gong, Q. Zhou, X. Feng, J. Fan, Q. Xiang, Crystalline isotype heptazine-/triazine-based carbon nitride heterojunctions for an improved hydrogen evolution, Appl. Catal. B Environ. 268 (2020), 118381.

[28] Z. Zhou, Y. Zhang, Y. Shen, S. Liu, Y. Zhang, Molecular engineering of polymeric carbon nitride: advancing applications from photocatalysis to biosensing and more, Chem. Soc. Rev. 47 (2018) 2298–2321.

[29] B.V. Lotsch, M. Döblinger, J. Sehnert, L. Seyfarth, J. Senker, O. Oeckler, W. Schnick, Unmasking melon by a complementary approach employing electron diffraction, solid-state NMR spectroscopy, and theoretical calculations—structural characterization of a carbon nitride polymer, Chem. Eur. J. 13 (2007) 4969–4980.

[30] Y. Kang, Y. Yang, L.C. Yin, X. Kang, L. Wang, G. Liu, H.M. Cheng, Selective breaking of hydrogen bonds of layered carbon nitride for visible light photocatalysis, Adv. Mater. 28 (2016) 6471–6477.

[31] B. Li, Y. Si, B.-X. Zhou, Q. Fang, Y.-Y. Li, W.-Q. Huang, W. Hu, A. Pan, X. Fan, G.-F. Huang, Doping-induced hydrogen-bond engineering in polymeric carbon nitride to significantly boost the photocatalytic H_2 evolution performance, ACS Appl. Mater. Interfaces 11 (2019) 17341–17349.

[32] D.B. Nimbalkar, M. Stas, S.-S. Hou, S.-C. Ke, J.-J. Wu, Microscopic revelation of charge-trapping sites in polymeric carbon nitrides for enhanced photocatalytic activity by correlating with chemical and electronic structures, ACS Appl. Mater. Interfaces 11 (2019) 19087–19095.

[33] W. Iqbal, B. Qiu, Q. Zhu, M. Xing, J. Zhang, Self-modified breaking hydrogen bonds to highly crystalline graphitic carbon nitrides nanosheets for drastically enhanced hydrogen production, Appl. Catal. B Environ. 232 (2018) 306–313.

[34] Y. Hu, Y. Shim, J. Oh, S. Park, S. Park, Y. Ishii, Synthesis of ^{13}C-, ^{15}N-labeled graphitic carbon nitrides and NMR-based evidence of hydrogen-bonding assisted two-dimensional assembly, Chem. Mater. 29 (2017) 5080–5089.

[35] X. Li, I.V. Sergeyev, F. Aussenac, A.F. Masters, T. Maschmeyer, J.M. Hook, Dynamic nuclear polarization NMR spectroscopy of polymeric carbon nitride photocatalysts: insights into structural defects and reactivity, Angew. Chem. Int. Ed. 130 (2018) 6964–6968.

[36] S. Yang, Y. Gong, J. Zhang, L. Zhan, L. Ma, Z. Fang, R. Vajtai, X. Wang, P. M. Ajayan, Exfoliated graphitic carbon nitride nanosheets as efficient catalysts for hydrogen evolution under visible light, Adv. Mater. 25 (2013) 2452–2456.

[37] P. Jiménez-Calvo, C. Marchal, T. Cottineau, V. Caps, V. Keller, Influence of the gas atmosphere during the synthesis of g-C_3N_4 for enhanced photocatalytic H_2 production from water on Au/g-C_3N_4 composites, J. Mater. Chem. A 7 (2019) 14849–14863.

[38] J. Oh, Y. Shim, S. Lee, S. Park, D. Jang, Y. Shin, S. Ohn, J. Kim, S. Park, Structural insights into photocatalytic performance of carbon nitrides for degradation of organic pollutants, J. Solid State Chem. 258 (2018) 559–565.

[39] H. Kim, D. Jang, S. Choi, J. Kim, S. Park, Acid-activated carbon nitrides as photocatalysts for degrading organic pollutants under visible light, Chemosphere 273 (2021), 129731.

[40] X. Li, S.T. Melissen, T. Le Bahers, P. Sautet, A.F. Masters, S.N. Steinmann, T. Maschmeyer, Shining light on carbon nitrides: leveraging temperature to understand optical gap variations, Chem. Mater. 30 (2018) 4253–4262.

[41] U. Holzwarth, N. Gibson, The Scherrer equation versus the 'Debye-Scherrer equation', Nat. Nanotechnol. 6 (2011), 534-534.

[42] H. Gong, S. Tang, T. Zhang, Catalytic hydrolysis of waste residue from the melamine process and the kinetics of melamine hydrolysis in NaOH solution, React. Kinet. Mech. Catal. 118 (2016) 377–391.

[43] A.M. Bernhard, D. Peitz, M. Elsener, A. Wokaun, O. Kröcher, Hydrolysis and thermolysis of urea and its decomposition byproducts biuret, cyanuric acid and melamine over anatase TiO_2, Appl. Catal. B Environ. 115 (2012) 129–137.

[44] B. Choudhury, P. Giri, Isotype heterostructure of bulk and nanosheets of graphitic carbon nitride for efficient visible light photodegradation of methylene blue, RSC Adv. 6 (2016) 24976–24984.

[45] C. Zhao, Q. Li, Y. Xie, L. Zhang, X. Xiao, D. Wang, Y. Jiao, C.A.H. Price, B. Jiang, J. Liu, Three-dimensional assemblies of carbon nitride tubes as nanoreactors for enhanced photocatalytic hydrogen production, J. Mater. Chem. A 8 (2020) 305–312.

[46] Y. Chen, B. Wang, S. Lin, Y. Zhang, X. Wang, Activation of n → π* transitions in two-dimensional conjugated polymers for visible light photocatalysis, J. Phys. Chem. C. 118 (2014) 29981–29989.

[47] D. Zhao, Y. Wang, C.-L. Dong, Y.-C. Huang, J. Chen, F. Xue, S. Shen, L. Guo, Boron-doped nitrogen-deficient carbon nitride-based Z-scheme heterostructures for photocatalytic overall water splitting, Nat. Energy 6 (2021) 388–397.

[48] M.K. Chee, C.-C. Er, J.-Y. Tang, L.-L. Tan, W.S. Chang, S.-P. Chai, Tuning the electronic band structure of graphitic carbon nitride by breaking intramolecular bonds: A simple and effective approach for enhanced photocatalytic hydrogen production, Appl. Surf. Sci. 529 (2020), 146600.

[49] X. Song, X. Zhang, X. Li, H. Che, P. Huo, C. Ma, Y. Yan, G. Yang, Enhanced light utilization efficiency and fast charge transfer for excellent CO_2 photoreduction activity by constructing defect structures in carbon nitride, J. Colloid Interface Sci. 578 (2020) 574–583.

[50] B. Choudhury, K.K. Paul, D. Sanyal, A. Hazarika, P. Giri, Evolution of nitrogen-related defects in graphitic carbon nitride nanosheets probed by positron annihilation and photoluminescence spectroscopy, J. Phys. Chem. C 122 (2018) 9209–9219.

[51] R. Godin, Y. Wang, M.A. Zwijnenburg, J. Tang, J.R. Durrant, Time-resolved spectroscopic investigation of charge trapping in carbon nitrides photocatalysts for hydrogen generation, J. Am. Chem. Soc. 139 (2017) 5216–5224.

[52] M. Thommes, K. Kaneko, A.V. Neimark, J.P. Olivier, F. Rodriguez-Reinoso, J. Rouquerol, K.S. Sing, Physisorption of gases, with special reference to the evaluation of surface area and pore size distribution (IUPAC Technical Report), Pure Appl. Chem. 87 (2015) 1051–1069.

[53] Y. Shiraishi, Y. Kofuji, S. Kanazawa, H. Sakamoto, S. Ichikawa, S. Tanaka, T. Hirai, Platinum nanoparticles strongly associated with graphitic carbon nitride as efficient co-catalysts for photocatalytic hydrogen evolution under visible light, Chem. Commun. 50 (2014) 15255–15258.